

# The Temperature-Dependent Viscoelastic Behavior of Dielectric Elastomers

**Jingkai Guo**

Department of Mechanical Engineering,  
The Johns Hopkins University,  
Baltimore, MD 21218  
e-mail: jguo19@jhu.edu

**Rui Xiao**

Department of Mechanical Engineering,  
The Johns Hopkins University,  
Baltimore, MD 21218  
e-mail: rxiao4@jhu.edu

**Harold S. Park**

Department of Mechanical Engineering,  
Boston University,  
Boston, MA 02215  
e-mail: parkhs@bu.edu

**Thao D. Nguyen<sup>1</sup>**

Department of Mechanical Engineering,  
The Johns Hopkins University,  
Baltimore, MD 21218  
e-mail: vicky.nguyen@jhu.edu

*In this paper, we investigated the temperature-dependent viscoelastic behavior of dielectric elastomers (DEs) and the effects of viscoelasticity on the electro-actuation behavior. We performed dynamic thermomechanical analysis to measure the master curve of the stress relaxation function and the temperature dependence of the relaxation time of VHB 4905, a commonly used DE. The master curve was applied to calculate the viscoelastic spectrum for a discrete multiprocess finite deformation viscoelastic model. In addition, we performed uniaxial creep and stress relaxation experiments and electrical actuation experiments under different prestretch conditions. The measured spectrum was applied to predict the experimental results. Generally, the model produced good quantitative agreement with both the viscoelastic and electro-actuation experiments, which shows the necessity of using a multiprocess relaxation model to accurately capture the viscoelastic response for VHB. However, the model underpredicted the electro-actuated creep strain for high voltages near the pull-in instability. We attributed the discrepancies to the complex boundary conditions that were not taken into account in the simulation. We also investigated the failure of VHB membrane caused by viscoelastic creep when pre-stretched and subjected to constant voltage loading. The experimental time to failure for the specimens decreased exponentially with voltage, which agreed well with the predictions of the model. [DOI: 10.1115/1.4030850]*

## 1 Introduction

DEs can deform when exposed to an applied electric field. The materials are capable of large deformation and have highly attractive features such as fast response, light weight, low cost, and good electromechanical conversion efficiency [1,2]. When pre-stretched and sandwiched between two compliant electrodes, DE membranes have demonstrated voltage-induced areal expansions up to 158% [3]. These features make DEs attractive for soft robotic actuators [4–6], artificial limbs [7,8], energy harvesters [9,10], adaptive optics [11–13], Braille displays [14], and biostimulation pads [15,16].

Applying an electric field across the thickness of a DE generates a Maxwell stress that reduces the thickness of the film and causes the area to expand. As the elastomer thins, applying the same voltage leads to an increasing higher electric field. This positive feedback between deformation and electric field can lead to failure by pull-in instability and dielectric breakdown. When the film becomes unstable, complex 3D wrinkling patterns appear [17]. It has been revealed that prestretches can help to eliminate the pull-in instability [18] and improve electric breakdown strength [19,20].

The elastic behavior of DEs has been studied extensively [21–24], and the viscoelastic behavior of this material has gained increased scrutiny in recent works [25,26]. Experiments have shown that viscoelasticity can significantly affect the electromechanical behavior. It has been observed in experiments that viscoelastic creep under a constant voltage actuation can induce the pull-in instability and electric breakdown [27]. Failure caused by pull-in instability and dielectric strength is a major limitation in the application of DEs. Therefore, accurate characterization of the viscoelastic behavior is important for the development of dielectric devices. Zhang and Chen proposed a viscoelastic model for the DE balloon using free-energy method [28]. Zhao et al.

developed a nonequilibrium thermodynamic theory for the viscoelastic behavior of DEs [29]. Park and Nguyen developed a dynamic finite element method to investigate the effect of viscoelasticity on the development of instabilities and electromechanical actuation [30,31]. Lochmatter et al. [32] developed a viscohyperelastic model to study a DE strip actuator under sinusoidal excitation. Yang et al. [33] developed a nonlinear finite deformation viscoelastic model of dielectric membranes using Christensen's theory of viscoelasticity. Wissler and Mazza [34] used quasi-linear viscoelastic constitutive models with different energy formulations to predict creep behavior of VHB under different voltage levels. Recently, Kollosche et al. [35] applied a single process viscoelastic model to study the wrinkle-to-wrinkle transition of DEs.

Viscoelastic models of DEs typically apply a single relaxation process to describe the creep, stress relaxation, and rate-dependent stress response over a narrow range of time scales [29,35]. A few models have applied multiple relaxation processes [30,34,36], up to 4, to describe a wider range of behavior and time scales, such  $10^{-1}$ – $10^3$  s. The parameters for the relaxation times and moduli were fit to mechanical creep or stress relaxation data [36] or voltage-induced electrical actuation data [34]. These approaches are limited in that they do not describe completely the broad distribution of relaxation processes nor the temperature dependence of the viscoelastic behavior. Michel et al. measured the elastic modulus of VHB 4910 by uniaxial tension experiments in different temperatures and observed a strong temperature dependence [37]. The aim of this work was to characterize the temperature-dependent viscoelastic spectrum of VHB, a widely used commercial DE. We applied the principles of time-temperature superposition (TTS) to construct the master curve of the relaxation modulus from relaxation tests at different temperatures. The master curve was applied to calculate the viscoelastic spectrum and temperature dependence of the relaxation times for a discrete multiprocess viscoelastic model. We performed standard viscoelastic experiments (creep and stress relaxation) as well as voltage actuation experiments on VHB membranes. The measured spectrum was applied to simulate these experiments as well

<sup>1</sup>Corresponding author.

Contributed by the Applied Mechanics Division of ASME for publication in the JOURNAL OF APPLIED MECHANICS. Manuscript received May 4, 2015; final manuscript received June 12, 2015; published online June 25, 2015. Editor: Yonggang Huang.

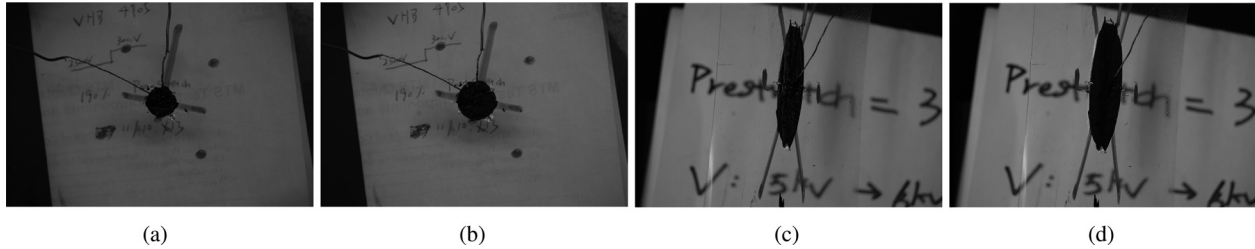


**Fig. 1** Images taken from actuation experiments: (a) and (b) equibiaxial prestretch, before and after actuation, and (c) and (d) uniaxial prestretch, before and after actuation

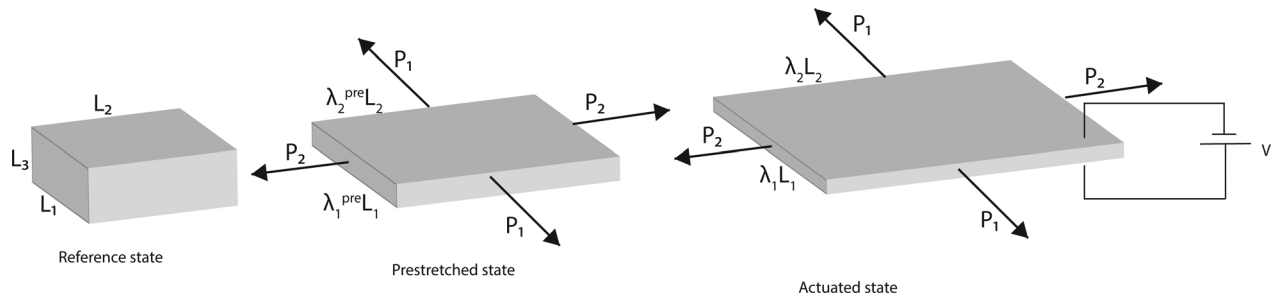


**Fig. 2** Model of electromechanical couple of DE membrane

as experiments performed in Refs. [17,27] to validate the model. Finally, we introduced an approach to selectively reduce and truncate the viscoelastic spectrum for a given time scale and temperature for computational efficiency, and demonstrated the shifting the spectrum to describe the viscoelastic behavior at different temperatures.

## 2 Methods

**2.1 Experimental Method.** Commercially available VHB 4905 membranes (3M, St. Paul, MN) were used in all experiments. The membrane was cut to different sizes, described in below, according to needs of experiments.

**2.1.1 Uniaxial Creep and Stress Relaxation Experiments.** The creep and stress relaxation response of VHB was measured using a dynamic mechanical analyzer (DMA TA Q800, TA Instruments, Newcastle, DE). Film specimens, 15 mm long, 6.0 mm wide, and 0.5 mm thick, were cut from the VHB 4905 tape and mounted in the film tension grips of the DMA leaving an 8.0 mm gauge length.

The stress relaxation response was measured at different temperatures to construct the master curve of the relaxation modulus. The temperature was decreased from 60 °C to -40 °C in steps of 5 °C. Each temperature step was held for 15 min to reach thermal equilibrium. The specimens were stretched at a strain rate of 1%/s by 0.01 and held at 0.01 strain while the stress was measured for 20 min. The relaxation modulus was calculated as the uniaxial engineering stress divided by the applied strain and was plotted as function of time. The relaxation modulus measured at different temperatures was horizontally shifted to the reference temperature 20 °C, according to the principles of the TTS, to form a master curve for the time-dependent relaxation modulus. Specifically, we defined a function  $\alpha(T)$  for the temperature-dependent shift factor. To determine the shift factor at the temperature  $T$ , the relaxation modulus measured at  $T$  was shifted along the horizontal log-time axis by the logarithm of the shift factor,  $\log \alpha(T)$ , to join the curves for the relaxation modulus generated by data from previous temperatures. The logarithmic shift factor was  $\log \alpha(T) < 0$  for temperatures lower than the reference temperature and  $\log \alpha(T) > 0$  for temperatures higher than the reference temperature. Shift factors were adjusted until all data points formed a continuous, smooth master curve at the reference temperature.

We performed additional stress relaxation experiments at large strains and creep experiments for model validation. For the stress relaxation experiments, the film specimens were equilibrated at 20 °C, stretched to 100% strain at a rate of 12.5%/s, and relaxed for 2 hrs. For the creep experiments, film specimens were equilibrated at 20 °C and subjected to a uniaxial force, which linearly increased from zero to 0.17 N with a loading rate of 0.01 N/s and then held for 6 hrs. Uniaxial stretch during creep was recorded as a function of time.

**2.1.2 Electrical Actuation Experiments.** Square specimens ranging from 63.5 mm to 127 mm in size were cut from the VHB tape. The side length was decided according to the prestretch level that would be applied in a particular experiment. A cross was drawn in the center of the film and four points were drawn around the cross and used as optical markers to measure the prestretch applied in the experiments. The specimen was uniaxially or equibiaxially stretched to the desired prestretch and attached to a rigid frame which is a square with side length of 190.5 mm. VHB is an adhesive tape, which provided a strong attachment to the frame. A circular electrode made from carbon conductive grease (846-1P, MG Chemicals, Surrey, BC, Canada) with a diameter of 10 mm was applied to the center of the prestretched film on both sides. The area of the central electrode was relatively small compared to the dimensions of the prestretched specimen. The prestretched film was allowed to relax 1.5 hrs to reach an equilibrium stress state. A voltage was applied across the electrodes using a high voltage power supply (ES50P-5 W, Gamma High Voltage Research, Ormond Beach, FL). The experiments investigated applied voltages from 2.5 kV to 6 kV. A digital camera mounted above specimens was used to image the deforming specimens every 8 s to 20 s. The images were analyzed using GIMP<sup>2</sup> to measure the major and minor axes of the deformed electrode (Fig. 1). The principal stretches were calculated from the ratio of deformed major and minor axes to the undeformed diameter of the electrode.

**2.2 Constitutive Model.** We applied the analytical model developed by Suo [38] to describe the viscoelastic biaxial stress response of an incompressible DE membrane subjected to an equilibrium prestretch and a sudden applied voltage change (Fig. 2). The biaxial stress state was characterized by in-plane stretches  $\lambda_1$  and  $\lambda_2$ ,

<sup>2</sup>[www.gimp.org](http://www.gimp.org)

and an out-of-plane stretch  $\lambda_3$ . For membrane with applied pre-stretch  $\lambda_1^{\text{pre}}$  and  $\lambda_2^{\text{pre}}$ , we can define relative stretches as  $\lambda_1^{\text{rel}} = \lambda_1/\lambda_1^{\text{pre}}$ ,  $\lambda_2^{\text{rel}} = \lambda_2/\lambda_2^{\text{pre}}$  which represent stretches purely from electric actuation.

In the model, we assumed that VHB 4905 is an incompressible and isotropic material. Thus,  $\lambda_3 = \lambda_1^{-1}\lambda_2^{-1}$ . The permittivity of the material was assumed to be  $\varepsilon = 3.98 \times 10^{-11}$  F/m [19], which gave a dielectric constant of  $\varepsilon_d = 4.5$ . We also assumed that the permittivity is independent of deformation for simplicity. Previous studies have assumed both a linear and nonlinear dependence on deformation [39,40]. Moreover, we assumed that VHB is an ideal DE, such that the total free-energy density of DEs can be decomposed into mechanical and electrical parts

$$W = W_{\text{mech}} + W_e \quad (1)$$

The electrical contribution to the free-energy density is described by a quadratic potential

$$W_e = \varepsilon E^2/2 \quad (2)$$

where  $E$  is electrical field. The electric displacement is given as  $D = \varepsilon E$ .

The electric field energy density of ideal DE can be written in terms of the nominal electric field  $\tilde{E}$  and electric displacement  $\tilde{D}$  as

$$W_e = \frac{\tilde{D}^2}{2\varepsilon} \lambda_1^{-2} \lambda_2^{-2} = \frac{\varepsilon \tilde{E}^2}{2} \lambda_1^2 \lambda_2^2 \quad (3)$$

The mechanical behavior of the DE is described by the multiprocess viscoelastic model illustrated in Fig. 3. The model consists of a parallel distribution of Maxwell models acting in parallel with an equilibrium spring. The equilibrium spring is characterized by an equilibrium shear modulus of  $\mu^{\text{eq}}$ , while the Maxwell models are described by a shear modulus of  $\mu_k^{\text{neq}}$  and relaxation time of  $\tau_k$ . The temperature dependence of the relaxation time was described as  $\tau_k(T) = \tau_k^{\text{ref}} \alpha(T)$ , where  $\tau_k^{\text{ref}}$  is the relaxation time at the reference temperature (20 °C), and  $\alpha(T)$  is the shift factor measured in Sec. 2.1.1. We assumed a multiplicative decomposition of the deformation gradient into elastic  $\lambda_{1e}^k$  and viscous components  $\xi_2^k$ , such that  $\lambda_{1e}^k = \lambda_1/\xi_1^k$ ,  $\lambda_{2e}^k = \lambda_2/\xi_2^k$ . The  $N$  relaxation processes represent a discrete approximation of a continuous distribution of relaxation times. Using a larger number  $N$  of processes provides a more accurate description of the time-dependent relaxation behavior at the expense of computational time. In Sec. 2.3, we present a method to determine the parameters of the relaxation spectrum from the master curve of the relaxation modulus. We also investigated, in Sec. 3.4, the effect of coarsening and altering the range of the discrete relaxation spectrum on the simulation results of the viscoelastic behavior of VHB.

We assumed that the mechanical strain energy density can be additively split into equilibrium and nonequilibrium components,  $W_{\text{mech}}(\lambda_1, \lambda_2, \xi_1^k, \xi_2^k) = W_{\text{mech}}^{\text{eq}}(\lambda_1, \lambda_2) + \sum W_{\text{mech}}^{\text{neq}}(\lambda_{1e}^k, \lambda_{2e}^k)$ . We adopted the Gent model for both the equilibrium and nonequilibrium components to describe for the stiffening of the material when approaching the limiting stretch [41]

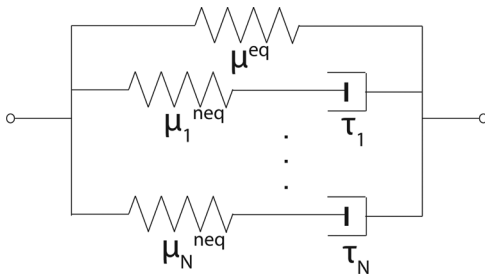


Fig. 3 Standard rheological model

$$W_{\text{mech}} = -\frac{\mu^{\text{eq}} J_{\text{lim}}^{\text{eq}}}{2} \log \left( 1 - \frac{\lambda_1^2 + \lambda_2^2 + \lambda_1^{-2} \lambda_2^{-2} - 3}{J_{\text{lim}}^{\text{eq}}} \right) - \sum_{k=1}^N \frac{\mu_k^{\text{neq}} J_{\text{lim}}^{\text{neq}}}{2} \times \log \left( 1 - \frac{\lambda_1^2 (\xi_1^k)^{-2} + \lambda_2^2 (\xi_2^k)^{-2} + \lambda_1^{-2} \lambda_2^{-2} (\xi_1^k \xi_2^k)^2 - 3}{J_{\text{lim}}^{\text{neq}}} \right) \quad (4)$$

where  $J_{\text{lim}}^{\text{eq}}$  and  $J_{\text{lim}}^{\text{neq}}$  are the limiting stretches of the equilibrium spring and nonequilibrium components,  $\xi_1^k$  and  $\xi_2^k$  denote  $k$ th viscous stretches in two in-plane principle directions. We have assumed that the nonequilibrium processes share the same limiting stretch  $J_{\text{lim}}^{\text{neq}}$  for simplicity. This model is an extension of the viscoelastic models developed by Zhao et al. [29] and Park and Nguyen [30] that used a single exponential relaxation process to describe the viscoelastic behavior. Substituting Eqs. (3) and (4) into Eq. (1) gives the total free-energy density function. The principal first Piola–Kirchhoff engineering stresses were defined from the free-energy density as [38]

$$s_1 = \frac{\partial W(\lambda_1, \lambda_2, \xi_1^k, \xi_2^k, \tilde{D})}{\partial \lambda_1} \quad (5)$$

$$s_2 = \frac{\partial W(\lambda_1, \lambda_2, \xi_1^k, \xi_2^k, \tilde{D})}{\partial \lambda_2}$$

where  $s_1 = (P_1/L_2L_3) = (\sigma_1/\lambda_1)$  and  $s_2 = (P_2/L_1L_3) = (\sigma_2/\lambda_2)$  are engineering stresses in two principle directions. Evaluating Eq. (5) and applying the relation between the engineering and Cauchy stresses gives

$$\sigma_1 + \varepsilon E^2 = \frac{\mu^{\text{eq}} (\lambda_1^2 - \lambda_1^{-2} \lambda_2^{-2})}{1 - (\lambda_1^2 + \lambda_2^2 + \lambda_1^{-2} \lambda_2^{-2} - 3)/J_{\text{lim}}^{\text{eq}}} + \sum_{k=1}^N \frac{\mu_k^{\text{neq}} [\lambda_1^2 (\xi_1^k)^{-2} - \lambda_1^{-2} \lambda_2^{-2} (\xi_1^k \xi_2^k)^2]}{1 - [\lambda_1^2 (\xi_1^k)^{-2} + \lambda_2^2 (\xi_2^k)^{-2} + \lambda_1^{-2} \lambda_2^{-2} (\xi_1^k \xi_2^k)^2 - 3]/J_{\text{lim}}^{\text{neq}}} \times \frac{\mu_k^{\text{neq}} [\lambda_1^2 (\xi_1^k)^{-2} - \lambda_1^{-2} \lambda_2^{-2} (\xi_1^k \xi_2^k)^2]}{1 - [\lambda_1^2 (\xi_1^k)^{-2} + \lambda_2^2 (\xi_2^k)^{-2} + \lambda_1^{-2} \lambda_2^{-2} (\xi_1^k \xi_2^k)^2 - 3]/J_{\text{lim}}^{\text{neq}}}$$

$$\sigma_2 + \varepsilon E^2 = \frac{\mu^{\text{eq}} (\lambda_2^2 - \lambda_1^{-2} \lambda_2^{-2})}{1 - (\lambda_1^2 + \lambda_2^2 + \lambda_1^{-2} \lambda_2^{-2} - 3)/J_{\text{lim}}^{\text{eq}}} + \sum_{k=1}^N \frac{\mu_k^{\text{neq}} [\lambda_2^2 (\xi_2^k)^{-2} - \lambda_1^{-2} \lambda_2^{-2} (\xi_1^k \xi_2^k)^2]}{1 - [\lambda_1^2 (\xi_1^k)^{-2} + \lambda_2^2 (\xi_2^k)^{-2} + \lambda_1^{-2} \lambda_2^{-2} (\xi_1^k \xi_2^k)^2 - 3]/J_{\text{lim}}^{\text{neq}}} \times \frac{\mu_k^{\text{neq}} [\lambda_2^2 (\xi_2^k)^{-2} - \lambda_1^{-2} \lambda_2^{-2} (\xi_1^k \xi_2^k)^2]}{1 - [\lambda_1^2 (\xi_1^k)^{-2} + \lambda_2^2 (\xi_2^k)^{-2} + \lambda_1^{-2} \lambda_2^{-2} (\xi_1^k \xi_2^k)^2 - 3]/J_{\text{lim}}^{\text{neq}}} \quad (6)$$

Following Ref. [42], we apply the following evolution equation for the viscous stretches:

$$\eta_k \frac{d\xi_i^k}{\xi_i^k dt} = \frac{1}{2} \sigma_{ik}^{\text{neq}}, \quad \text{for } i = 1, 2 \quad (7)$$

where  $\eta_k(T) = \mu_k^{\text{neq}} \tau_k(T) = \mu_k^{\text{neq}} \tau_k^{\text{ref}} \alpha(T)$  is the shear viscosity,  $\sigma_{ik}^{\text{neq}}$  is the nonequilibrium deviatoric component of the Cauchy stress in Eq. (6) and can be written as

$$\sigma_{1k}^{\text{neq}} = \frac{1}{3} \left( \frac{2[\lambda_1^2 (\xi_1^k)^{-2} - \lambda_1^{-2} \lambda_2^{-2} (\xi_1^k \xi_2^k)^2]}{1 - [\lambda_1^2 (\xi_1^k)^{-2} + \lambda_2^2 (\xi_2^k)^{-2} + \lambda_1^{-2} \lambda_2^{-2} (\xi_1^k \xi_2^k)^2 - 3]/J_{\text{lim}}^{\text{neq}}} - \frac{[\lambda_2^2 (\xi_2^k)^{-2} - \lambda_1^{-2} \lambda_2^{-2} (\xi_1^k \xi_2^k)^2]}{1 - [\lambda_1^2 (\xi_1^k)^{-2} + \lambda_2^2 (\xi_2^k)^{-2} + \lambda_1^{-2} \lambda_2^{-2} (\xi_1^k \xi_2^k)^2 - 3]/J_{\text{lim}}^{\text{neq}}} \right) \mu_k^{\text{neq}}$$

$$\sigma_{2k}^{\text{neq}} = \frac{1}{3} \left( \frac{-[\lambda_1^2 (\xi_1^k)^{-2} - \lambda_1^{-2} \lambda_2^{-2} (\xi_1^k \xi_2^k)^2]}{1 - [\lambda_1^2 (\xi_1^k)^{-2} + \lambda_2^2 (\xi_2^k)^{-2} + \lambda_1^{-2} \lambda_2^{-2} (\xi_1^k \xi_2^k)^2 - 3]/J_{\text{lim}}^{\text{neq}}} + \frac{2[\lambda_2^2 (\xi_2^k)^{-2} - \lambda_1^{-2} \lambda_2^{-2} (\xi_1^k \xi_2^k)^2]}{1 - [\lambda_1^2 (\xi_1^k)^{-2} + \lambda_2^2 (\xi_2^k)^{-2} + \lambda_1^{-2} \lambda_2^{-2} (\xi_1^k \xi_2^k)^2 - 3]/J_{\text{lim}}^{\text{neq}}} \right) \mu_k^{\text{neq}} \quad (8)$$

To determine the criteria for pull-in instability, we calculated the Hessian matrix of the free-energy density function (1)

$$\mathbf{H} = \begin{bmatrix} \frac{\partial^2 W}{\partial \lambda_1^2} & \frac{\partial^2 W}{\partial \lambda_1 \partial \lambda_2} & \frac{\partial^2 W}{\partial \lambda_1 \partial \bar{D}} \\ \frac{\partial^2 W}{\partial \lambda_1 \partial \lambda_2} & \frac{\partial^2 W}{\partial \lambda_2^2} & \frac{\partial^2 W}{\partial \lambda_2 \partial \bar{D}} \\ \frac{\partial^2 W}{\partial \lambda_1 \partial \bar{D}} & \frac{\partial^2 W}{\partial \lambda_2 \partial \bar{D}} & \frac{\partial^2 W}{\partial \bar{D}^2} \end{bmatrix} \quad (9)$$

The components of  $\mathbf{H}$  are functions of  $\lambda_1, \lambda_2, \xi_1^k, \xi_2^k, \bar{D}$  and evolve with time. We used the following criteria for pull-in instability in our simulation [29]:

$$\det \mathbf{H} = 0 \quad (10)$$

**2.3 Parameters Determination.** The master curve of the relaxation modulus was used to determine the equilibrium shear modulus and the parameters of the discrete relaxation spectrum ( $\tau_k, \mu_k^{\text{neq}}$ ). We initially assumed a large number of relaxation processes,  $N = 30$ . The relaxation modulus measured at different temperature was plotted on a log-log scale in Fig. 4(a). The relaxation modulus was shifted horizontally to a reference temperature of 20 °C to form the master curve for the time-dependence of the relaxation modulus in (Fig. 4(b)). The material exhibited a broad glass relaxation spectrum, where the relaxation modulus spanned more than 13 decades of log time. The temperature dependence of shift factor can be described by the Williams–Landel–Ferry (WLF) empirical relation

$$\log \alpha(T) = \frac{-C_1^{\text{ref}}(T - T^{\text{ref}})}{C_2^{\text{ref}} + T - T^{\text{ref}}} \quad (11)$$

where  $C_1^{\text{ref}}$  and  $C_2^{\text{ref}}$  are the WLF constants for the reference temperature. Fitting the WLF relation to the shift factor data (Fig. 5) gave  $C_1^{\text{ref}} = 13.7$  and  $C_2^{\text{ref}} = 187.1$  °C. The equilibrium modulus  $E^{\text{eq}} = 0.078$  MPa was approximated from the plateau of the master curve at large times. Assuming incompressibility, the equilibrium shear modulus can be determined from the equilibrium Young's modulus as  $\mu^{\text{eq}} = E^{\text{eq}}/3 = 0.026$  MPa. The nonequilibrium  $E^{\text{neq}} = 689$  MPa was approximated by the maximum relaxation modulus of the master curve in Fig. 4(b) and applied to calculate the  $\mu^{\text{neq}} = 230$  MPa assuming incompressibility. Physically,  $\mu^{\text{neq}}$  represents the glassy modulus. However, we were unable to reach plateaus for the lowest temperature, -40 °C, of the stress relaxation tests. At room temperature 20 °C, the relaxation observed at

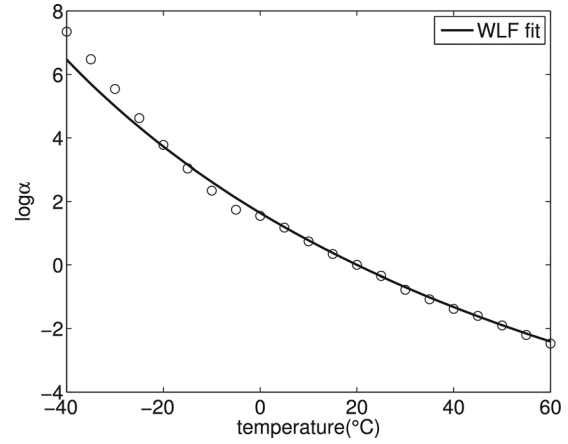


Fig. 5 Shift factor as a function of temperature

-40 °C corresponds to stress relaxation at  $10^{-7}$  s, which is significantly smaller than the experimental time scale. Consequently, truncating the master curve at  $10^{-7}$  s should not significantly affect the model predictions of material behavior and instability at room temperature.

We developed a second-order approximation method based on Schwarzl and Staverman [43] to determine the discrete relaxation spectrum [44]. A seventh-order polynomial was first fit to the master curve in Fig. 4(b). The resulting polynomial function was denoted as  $\log G = f_0(\log t)$ , where  $G$  is the relaxation modulus. The relationship between the relaxation modulus and a continuous relaxation spectrum was defined as [45]

$$G(t) = \mu^{\text{eq}} + \int_0^\infty \frac{h(\tau)}{\tau^2} e^{-t/\tau} d\tau \quad (12)$$

where  $h(\tau)$  is the continuous relaxation spectrum. The cumulative relaxation spectrum was defined from  $h(\tau)$  as

$$H(\tau) = \int_0^\tau h(z) dz \quad (13)$$

Evaluating  $h(\tau)$  requires inverting the integral equation (12), which can be challenging. A number of approximations have been developed. In particular, we used a second-order accurate approximation developed by Schwarzl and Staverman [43]

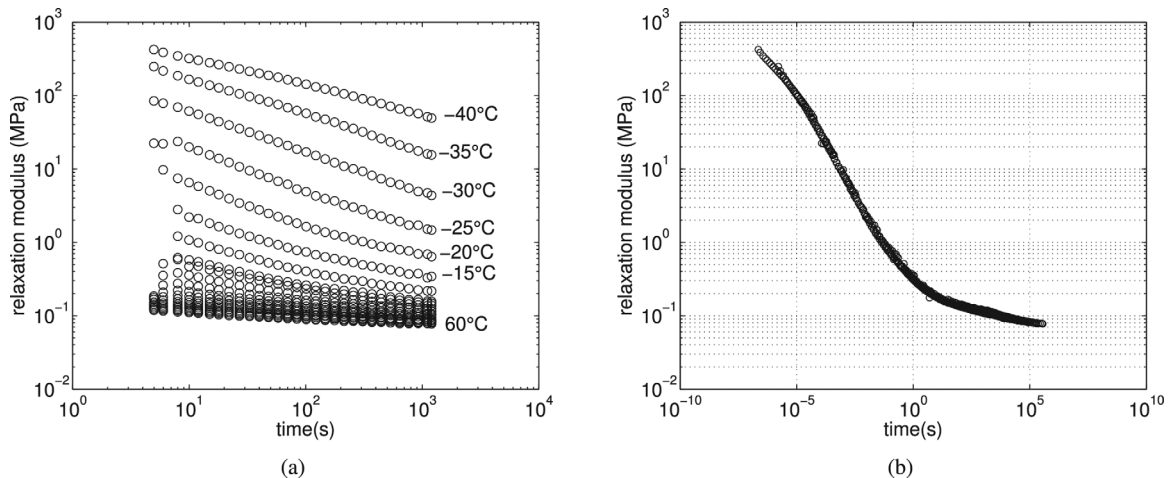
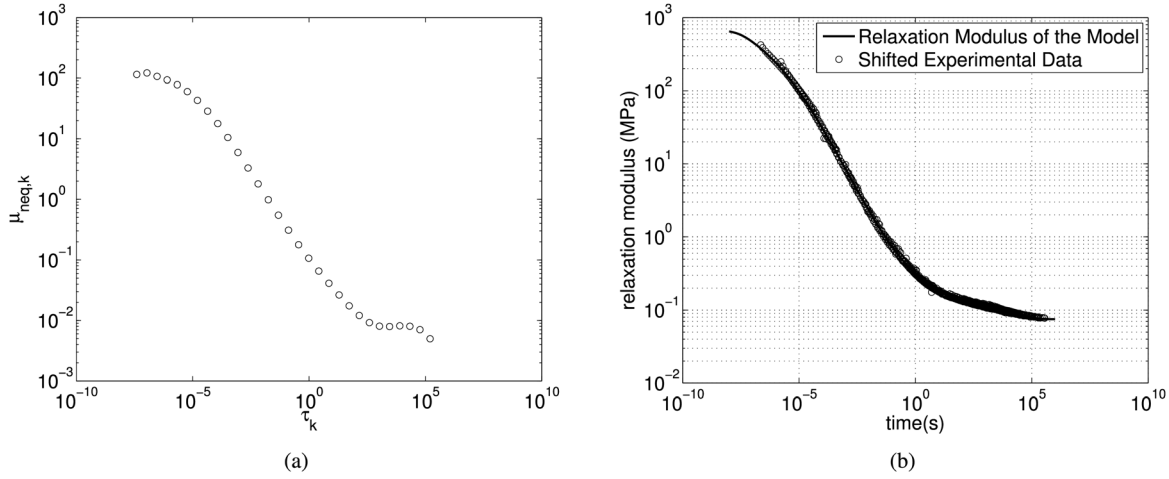


Fig. 4 Relaxation modulus as a function of time: (a) measured for different temperature and (b) shifted to a reference temperature of 20 °C to form a master curve



**Fig. 6 (a) Distribution of discrete viscoelastic spectrum  $(\tau_k, \mu_k^{\text{neq}})$ . (b) Comparison between master curves from experiments and the discrete model.**

$$h(\tau) = -\frac{t}{2} G(t) [d \log G(t) / d \log t - (d \log G(t) / d \log t)^2 - (1/2.303)d^2 \log G(t) / d(\log t)^2] \Big|_{t=2\tau} \quad (14)$$

Applying the polynomial fit to Eqs. (14) and (13), we can calculate the continuous relaxation spectrum and cumulative distribution from polynomial  $f_0$  as

$$h(\tau) = -\frac{1}{2} 10^{f_0(x)+x} (f_0'(x) - (f_0'(x))^2 - (1/2.303)f_0''(x)) \Big|_{x=\log 2\tau} \quad (15)$$

$$H(\tau) = 10^{f_0(x)} (1 - f_0'(x)) \Big|_{x=\log 2\tau} \quad (16)$$

The relaxation modulus of the discrete model can be written as assuming infinitesimal deformation as

$$G_{\text{disc}}(t) = \mu^{\text{eq}} + \sum_k^N \mu_k^{\text{neq}} \exp(-t/\tau_k) \quad (17)$$

The discrete cumulative spectrum can be evaluated by combining Eqs. (12), (13), and (17) as

$$H_{\text{disc}}(\tau) = \sum_k^N \mu_k^{\text{neq}} \langle \tau - \tau_k \rangle - \mu^{\text{eq}} \quad (18)$$

where  $\langle \tau - \tau_k \rangle = 0$  for  $\tau > \tau_k$ . A power law distribution was applied for relaxation time [46]

$$\tau_k = \tau_{\text{max}} \left( \frac{\tau_{\text{min}}}{\tau_{\text{max}}} \right)^{(k-1)/(N-1)} \quad (19)$$

The upper and lower bounds of relaxation distribution,  $\tau_{\text{max}} = 1.59 \times 10^5$  s and  $\tau_{\text{min}} = 3.98 \times 10^{-8}$  s, were determined according from the time range of master curve of the relaxation modulus (Fig. 4(b)). Finally, the nonequilibrium moduli  $\mu_k^{\text{neq}}$  corresponding to the relaxation times  $\tau_k$  were determined from the continuous cumulative distribution as follows [46,47]:

$$\begin{aligned} \mu_1^{\text{neq}} &= \frac{1}{2} (H(\tau_1) + H(\tau_2)) \\ \mu_k^{\text{neq}} &= \frac{1}{2} (H(\tau_{k+1}) - H(\tau_{k-1})), \quad 1 < k < N-1 \\ \mu_N^{\text{neq}} &= \mu^{\text{neq}} - \sum_k^{N-1} \mu_k^{\text{neq}} \end{aligned} \quad (20)$$

The discrete cumulative spectrum forms a stepwise approximation of the continuous cumulative spectrum. Figure 6(a) plots relaxation spectrum  $(\tau_k, \mu_k^{\text{neq}})$  determined as described above. Note that  $\mu_k^{\text{neq}}$  was maximum at the lower bound  $\tau_{\text{min}}$  of the distribution of relaxation times, which indicates that relaxation spectrum extends to relaxation times lower than the chosen  $\tau_{\text{min}}$ . However, relaxation times below the lower bound would relax too quickly to significantly affect the modeling results at room temperature. The spectrum was applied to Eq. (17) to evaluate the relaxation modulus of the discrete model. The results in Fig. 6(b) show excellent agreement with the measured master curve.

### 3 Results and Discussion

**3.1 Creep and Stress Relaxation.** The viscoelastic model was applied using parameters determined in Sec. 2.3 to simulate the creep and stress relaxation experiments described in Sec. 2.1.1. In addition, we used  $J_{\text{lim}}^{\text{eq}} = 110$ ,  $J_{\text{lim}}^{\text{neq}} = 55$  in the simulations based on the previous work of Foo et al. [48]. It was verified through numerical tests that the simulations were insensitive to  $J_{\text{lim}}^{\text{eq}}$  and  $J_{\text{lim}}^{\text{neq}}$ , which means changing these values has little effect on results presented in this paper. Figure 7(a) compares the results of the uniaxial stress relaxation experiment and simulation of VHB films stretched to 100% strain. The simulation used the same loading history prescribed in experiments. The stress response showed significant relaxation, decaying from 255 kPa to 52 kPa in 2 hrs. The modeling results showed good agreement with the stress relaxation measurements.

Figure 7(b) plots the creep response from experiments and modeling. The loading history of the experiment was applied for the simulations. The specimen exhibited significant creep throughout the experiment. The stretch increased nearly linearly in log time for the entire duration of the 6 hrs of the experiment. The model predictions showed good agreement with the creep measurements.

**3.2 Effect of Strain Rate.** Next, we applied the model and parameters determined in Sec. 2.3 to simulate the uniaxial stress experiments of VHB 4905 at different strain rates by Plante and Dubowsky [17]. Figure 8 compares model prediction and experimental for stretch rates  $3.3 \times 10^{-4}$ /s,  $9.4 \times 10^{-2}$ /s, and 1.8/s. The model accurately predicted the stress-strain response of VHB for the two lower stretch rates up to a stretch of 4. The largest discrepancy between the experimental data and model prediction was 18% and occurred for the highest stretch rate which was 1.8/s.

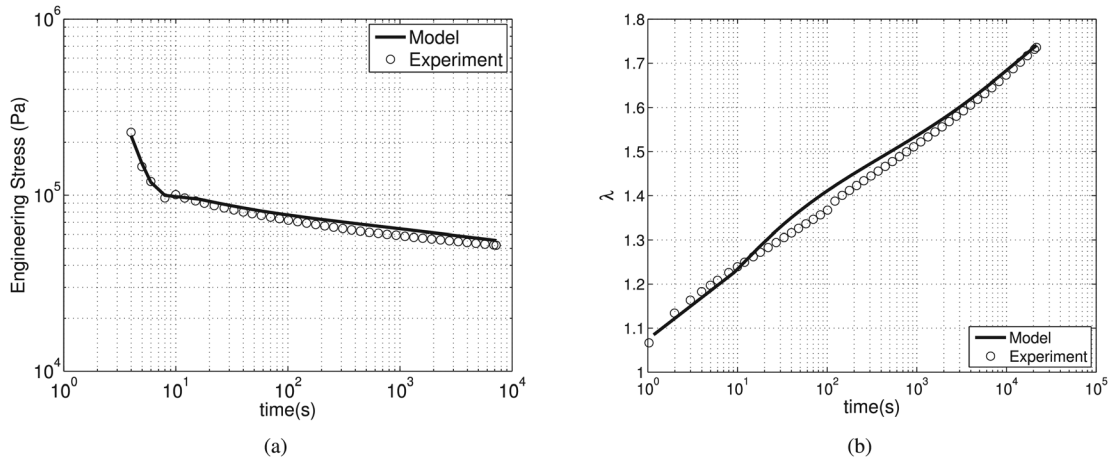


Fig. 7 (a) Relaxation of the uniaxial tension engineering stress response and (b) uniaxial tension creep stretch response, comparing experiments and model prediction

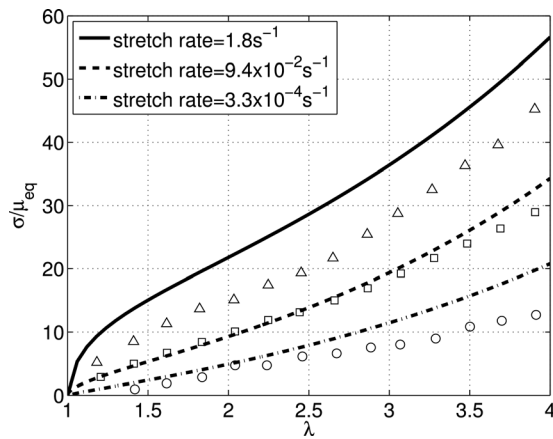


Fig. 8 Normalized stress as a function of stretch from uniaxial tension with different stretch rates, comparing experiments and model prediction

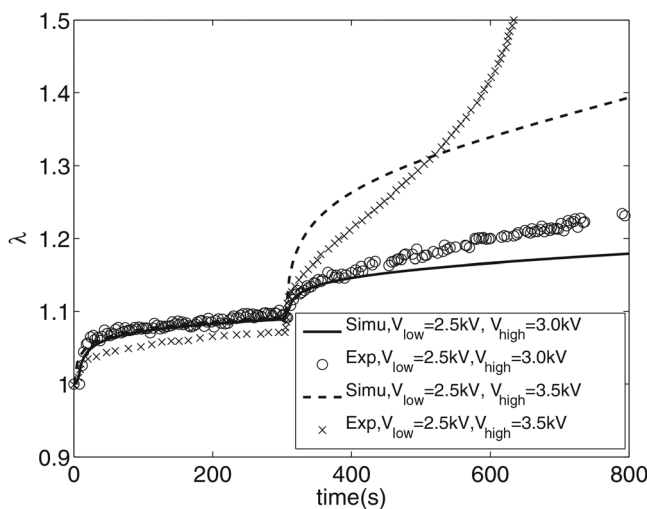


Fig. 9 Relative stretch as a function of time ( $\lambda_1^{\text{pre}} = \lambda_2^{\text{pre}} = 1.9$ ), comparing results from experiments and simulation

**3.3 Voltage-Induced Creep.** Figure 9 plots the relative stretch as a function of time for the electro-actuation of an equibiaxially prestretched membrane, comparing experiments in Sec. 2.1.2 and model predictions. In the experiments, the specimen was prestretched equibiaxially to 1.9, relaxed for 1.5 hrs, and then subjected to an applied voltage. The voltage was ramped from 0 to 2.5 kV in 10 s, held for 5 min, ramped to 3 kV in 10 s, and held until electric breakdown occurred. The loading history of the experiment was applied for the simulation. The electric field  $E$  was evaluated from the applied voltage as  $E = V/l_3$ , where  $l_3$  is the deformed thickness of the film, then applied to Eq. (6) to evaluate the equibiaxial stretch response. In addition, we simulated the electro-actuation experiments of Ref. [27], which subjected prestretched VHB membranes to the same prestretch,  $V_{\text{low}} = 2.5$  kV and a higher  $V_{\text{high}} = 3.5$  kV. Keplinger et al. [27] used a more accurate capacitive method to measure the stretch. The experiments and modeling results were compared in Fig. 9. The model predictions showed excellent agreement with experiments for the 2.5 kV step and also for the first 100 s of the 3.0 kV step. However, the model stretch prediction was significantly lower than experimental measurements near the onset of the pull-in instability observed by the accelerated creep rate.

**3.4 Reduced Representations of the Stress Relaxation Spectrum.** In Secs. 2.3–3.3, we used a large number of relaxation processes,  $N = 30$ , to guarantee accurate description of the viscoelastic response. However, the larger number of relaxation processes resulted in long computational times. In this section, we investigated the effect of reducing the number of processes on the modeling results for voltage-induced creep. The majority of the distribution of relaxation times at 20 °C fell below 1 s and should not significantly affect the long time electro-actuated creep response measured in the experiments. To demonstrate this, we determined the discrete spectrum for a reduced number  $N = 20$  of processes over the same span of relaxation times,  $\tau_{\text{min}} = 3.98 \times 10^{-8}$  s and  $\tau_{\text{max}} = 1.59 \times 10^5$  s. In addition, we evaluated the effects of using truncated relaxation spectrum with small number of processes,  $N = 10$ ,  $N = 5$ , and  $N = 3$ . To obtain the truncated spectrum, we first determined the relaxation spectrum for  $N_{\text{total}} = 13$  processes, then truncated this spectrum by picking the last ten processes for  $N = 10$ , the last five processes for  $N = 5$ , and the last three processes for  $N = 3$ . Thus, the truncated distribution spans  $\tau_{\text{min}} = 3.16 \times 10^{-5}$  s,  $\tau_{\text{max}} = 1.59 \times 10^4$  s for the  $N = 10$  case,  $\tau_{\text{min}} = 2.16$  s,  $\tau_{\text{max}} = 1.59 \times 10^4$  s for the  $N = 5$  case, and  $\tau_{\text{min}} = 185$  s,  $\tau_{\text{max}} = 1.59 \times 10^4$  s for the  $N = 3$  case. The different cases were summarized in Table 1 and the spectra were plotted in Fig. 10.

**Table 1 Parameters of spectra with different number of processes**

	$N$	$\tau_{\max}$ (s)	$\tau_{\min}$ (s)	$\mu^{\text{neq}}$ (MPa)
Case 1	30 (full range)	$1.59 \times 10^5$	$3.98 \times 10^{-8}$	230
Case 2	20 (full range)	$1.59 \times 10^5$	$3.98 \times 10^{-8}$	230
Case 3	10 (truncated)	$1.59 \times 10^4$	$3.16 \times 10^{-5}$	39.7
Case 4	5 (truncated)	$1.59 \times 10^4$	2.16	0.110
Case 5	3 (truncated)	$1.59 \times 10^4$	185	0.0247

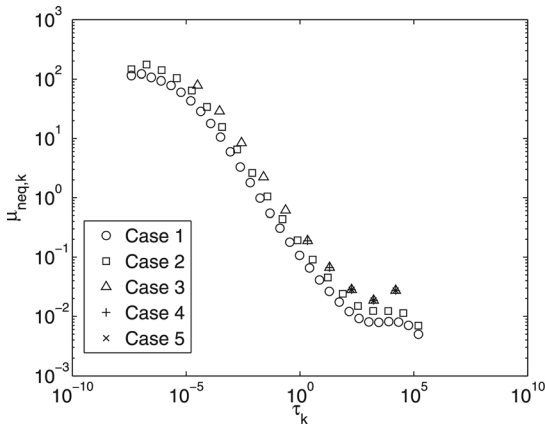


**Fig. 10 Distribution of discrete spectra for cases 1–5**

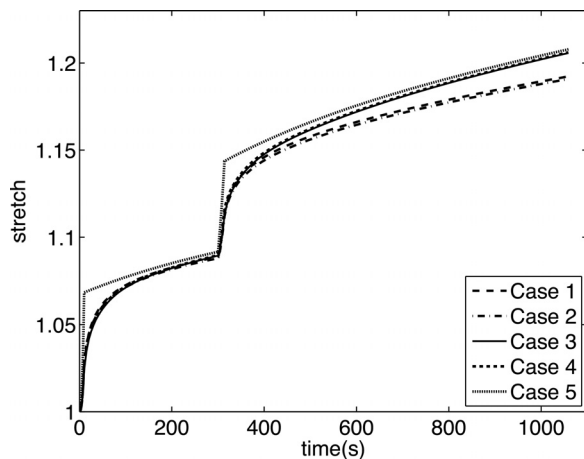


**Fig. 11 Voltage actuated creep simulation for cases 1–5 at 20°C**

The electro-actuation stretch response was computed for the five cases in Table 1 at room temperature  $T = 20^\circ\text{C}$ . The loading history was the same as introduced in Sec. 3.3 with  $V_{\text{low}} = 2.5\text{ kV}$  and  $V_{\text{high}} = 3.0\text{ kV}$ . The results in Fig. 11 for cases 1–4 showed negligible differences. The largest discrepancy among the first four cases was about 1%. Case 5 with only three nonequilibrium processes, however, cannot precisely describe the material’s short time response because of the truncation. This shows the importance of using multiple nonequilibrium processes to accurately capture the viscoelastic response of VHB, which is in contrast to the single relaxation process models that have been used to date [29,35].

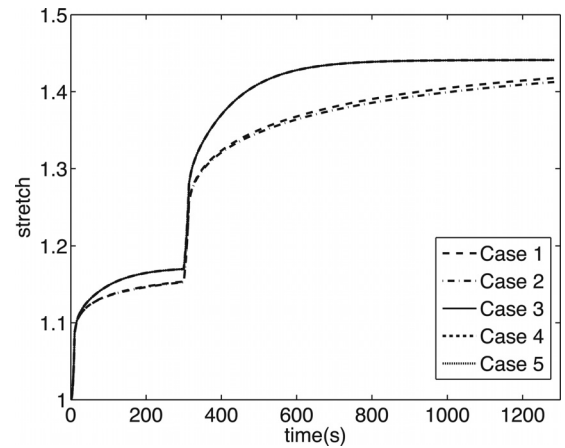


**Fig. 12 Voltage actuated creep simulation for cases 1–5 at 60°C**

The electro-actuation response was computed for a higher temperature,  $60^\circ\text{C}$  comparing all five cases (Fig. 12). The spectra for all cases were shifted to  $60^\circ\text{C}$  using the temperature-dependent shift factors shown in Fig. 5. Larger differences were observed between the truncated and full relaxation spectrum. The largest difference between the full and truncated spectrum was 5%. At high temperature, the VHB material became more mobile, and accurate predictions were needed for the relaxation processes with smaller relaxation times.

**3.5 Voltage-Induced Creep Failure.** As shown in Sec. 3.3, the model was unable to capture the accelerated creep at the onset of the pull-in instability. We attributed this discrepancy to the complex boundary conditions of the experiments, which were neglected in the simulations. The simulations assumed homogeneous deformation and a uniform biaxial stress state in the film. In experiments, the voltage was applied to a small region of the film, and the resulting electro-actuation caused the surrounding film to unload, which created a nonuniform deformation state.

We applied the model to investigate the effects of prestretch and voltage on the failure of DEs. The simulations considered two equibiaxial prestretch ratios, 1.7 and 1.9, and evaluated the time to creep-induced instability for different voltages. The criteria for pull-in instability were defined as  $\det \mathbf{H} = 0$ . In addition, we evaluated the time to electric breakdown for different voltages. The critical condition for electric breakdown was  $\lambda = \lambda_{\text{EB}}$ , where  $\lambda_{\text{EB}}$  is the breakdown stretch.

$$\lambda_{\text{EB}} = \sqrt{\frac{E_{\text{EB}} L_3}{V}} \quad (21)$$

where  $L_3$  represents the initial thickness and  $E_{\text{EB}}$  is the breakdown electric field. Kofod et al. [19] and Plante and Dubowsky [17] have measured  $E_{\text{EB}}$  as a function of prestretch. From their measurements, we used  $E_{\text{EB}} = 40\text{ MV/m}$  for a prestretch  $\lambda^{\text{pre}} = 1.7$  and  $E_{\text{EB}} = 48\text{ MV/m}$  for  $\lambda^{\text{pre}} = 1.9$ . Figures 13(a) and 13(b) plotted the voltage-induced relative strain for  $\lambda^{\text{pre}} = 1.7$  and  $\lambda^{\text{pre}} = 1.9$ . The time to break-down were marked using crosses on the curves in the figure, and the unstable limit points predicted from  $\det \mathbf{H} = 0$  were marked using circles. In all cases, breakdown happened before the pull-in instability which is coincident with our observations in the experiments that the stretch did not increase dramatically before electric breakdown occurred. Figure 13(c) compared the time to failure measured from experiments and calculated from the electric breakdown criteria for the model. The experiments and modeling results showed the same trends. The time to electric breakdown

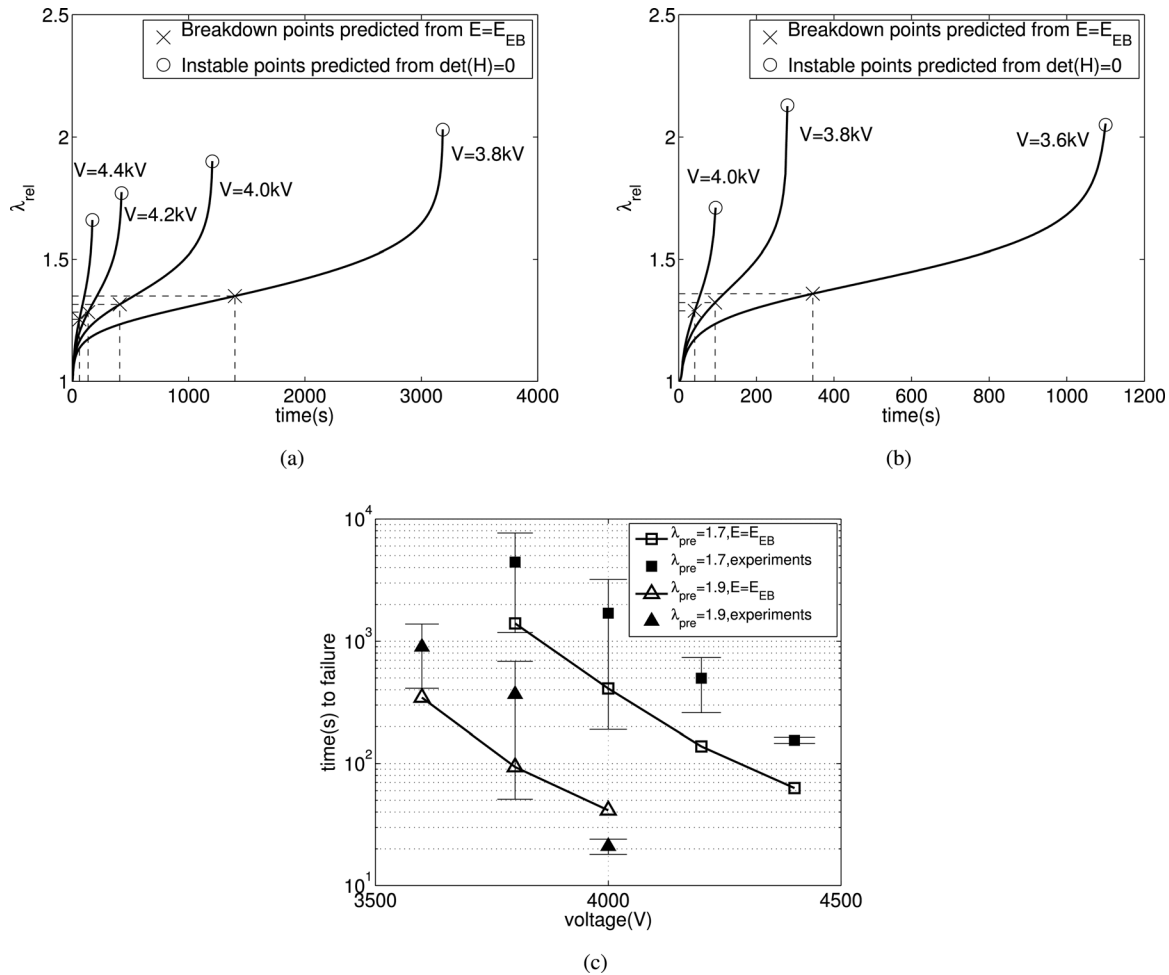


**Fig. 13** (a) Relative stretch from constant voltage actuation as a function of time,  $\lambda^{pre} = 1.7$ ,  $V = 3.8, 4.0, 4.2, 4.4\text{ kV}$ , (b) relative stretch from constant voltage actuation as a function of time,  $\lambda^{pre} = 1.9$ ,  $V = 3.6, 3.8, 4.0\text{ kV}$ , and (c) time to failure as a function of voltage

decreased exponentially with voltage (linearly in a semilog time). They also decreased with the prestretch.

#### 4 Conclusions

We measured the viscoelastic relaxation spectrum of VHB 4905 and the temperature dependence of the relaxation times and applied the results to a discrete multiprocess viscoelastic model. We showed that the viscoelastic spectrum can be truncated systematically to describe the time-dependent behavior in a more narrow time range, though the truncation was shown to require multiple and not a single nonequilibrium process in order to accurately capture the viscoelastic response. Moreover, the spectrum can be shifted using the temperature-dependent shift factor to describe the time-dependent behavior at higher temperatures. The model generally showed good quantitative agreement with experimental measurements of electromechanical behaviors. The model was able to qualitatively capture the dependence of the electric breakdown time with voltage and prestretch.

#### Acknowledgment

We thank Kailiang Ren of the Department of Material Science and Jonathan Wang of the Department of Mechanical Engineering at Johns Hopkins University for their assistance with the setup of the electrical actuation experiments. TDN and JG also acknowledge the funding support from the National Science Foundation (CMMI-1130358).

#### References

- [1] Brochu, P., and Pei, Q., 2010, "Advances in Dielectric Elastomers for Actuators and Artificial Muscles," *Macromol. Rapid Commun.*, **31**(1), pp. 10–36.
- [2] Anderson, I. A., Gisby, T. A., McKay, T. G., O'Brien, B. M., and Calius, E. P., 2012, "Multi-Functional Dielectric Elastomer Artificial Muscles for Soft and Smart Machines," *J. Appl. Phys.*, **112**(4), p. 041101.
- [3] Pelrine, R., Kornbluh, R., Pei, Q., and Joseph, J., 2000, "High-Speed Electrically Actuated Elastomers With Strain Greater Than 100%," *Science*, **287**(5454), pp. 836–839.
- [4] Pelrine, R., Kornbluh, R. D., Pei, Q., Stanford, S., Oh, S., Eckerle, J., Full, R. J., Rosenthal, M. A., and Meijer, K., 2002, "Dielectric Elastomer Artificial Muscle Actuators: Toward Biomimetic Motion," *Proc. SPIE*, **4695**, pp. 126–137.
- [5] Bar-Cohen, Y., 2004, *Electroactive Polymer (EAP) Actuators as Artificial Muscles*, SPIE Press, New York.
- [6] O'Halloran, A., O'Malley, F., and McHugh, P., 2008, "A Review on Dielectric Elastomer Actuators, Technology, Applications, and Challenges," *J. Appl. Phys.*, **104**(7), p. 071101.
- [7] Biddiss, E., and Chau, T., 2008, "Dielectric Elastomers as Actuators for Upper Limb Prosthetics: Challenges and Opportunities," *Med. Eng. Phys.*, **30**(4), pp. 403–418.
- [8] Ha, S. M., Yuan, W., Pei, Q., Pelrine, R., and Stanford, S., 2006, "Interpenetrating Polymer Networks for High-Performance Electroelastomer Artificial Muscles," *Adv. Mater.*, **18**(7), pp. 887–891.
- [9] Pelrine, R., Kornbluh, R. D., Eckerle, J., Jeuck, P., Oh, S., Pei, Q., and Stanford, S., 2001, "Dielectric Elastomers: Generator Mode Fundamentals and Applications," *Proc. SPIE*, **4329**, pp. 148–156.
- [10] Koh, S. J. A., Zhao, X., and Suo, Z., 2009, "Maximal Energy That Can be Converted by a Dielectric Elastomer Generator," *Appl. Phys. Lett.*, **94**(26), p. 262902.
- [11] Beck, M., Fiolka, R., and Stemmer, A., 2009, "Variable Phase Retarder Made of a Dielectric Elastomer Actuator," *Opt. Lett.*, **34**(6), pp. 803–805.



- [12] Kofod, G., Mc Carthy, D. N., Krissler, J., Lang, G., and Jordan, G., 2009, "Electroelastic Optical Fiber Positioning With Submicrometer Accuracy: Model and Experiment," *Appl. Phys. Lett.*, **94**(20), p. 202901.
- [13] Keplinger, C., Kaltenbrunner, M., Arnold, N., and Bauer, S., 2010, "Röntgen's Electrode-Free Elastomer Actuators Without Electromechanical Pull-In Instability," *Proc. Natl. Acad. Sci.*, **107**(10), pp. 4505–4510.
- [14] Bar-Cohen, Y., 2009, "Electroactive Polymers for Refreshable Braille Displays," *SPIE Newsroom* (epub).
- [15] Carpi, F., Frediani, G., and De Rossi, D., 2009, "Electroactive Elastomeric Haptic Displays of Organ Motility and Tissue Compliance for Medical Training and Surgical Force Feedback," *IEEE Trans. Biomed. Eng.*, **56**(9), pp. 2327–2330.
- [16] Carpi, F., Frediani, G., and De Rossi, D., 2010, "Hydrostatically Coupled Dielectric Elastomer Actuators for Tactile Displays and Cutaneous Stimulators," *Proc. SPIE*, **7642**, p. 76420E.
- [17] Plante, J.-S., and Dubowsky, S., 2006, "Large-Scale Failure Modes of Dielectric Elastomer Actuators," *Int. J. Solids Struct.*, **43**(25), pp. 7727–7751.
- [18] Koh, S. J. A., Li, T., Zhou, J., Zhao, X., Hong, W., Zhu, J., and Suo, Z., 2011, "Mechanisms of Large Actuation Strain in Dielectric Elastomers," *J. Polym. Sci., Part B: Polym. Phys.*, **49**(7), pp. 504–515.
- [19] Kofod, G., Sommer-Larsen, P., Kornbluh, R., and Pelrine, R., 2003, "Actuation Response of Polyacrylate Dielectric Elastomers," *J. Intell. Mater. Syst. Struct.*, **14**(12), pp. 787–793.
- [20] Kofod, G., 2008, "The Static Actuation of Dielectric Elastomer Actuators: How Does Pre-Stretch Improve Actuation?," *J. Phys. D: Appl. Phys.*, **41**(21), p. 215405.
- [21] Suo, Z., Zhao, X., and Greene, W. H., 2008, "A Nonlinear Field Theory of Deformable Dielectrics," *J. Mech. Phys. Solids*, **56**(2), pp. 467–486.
- [22] Lu, T., Huang, J., Jordi, C., Kovacs, G., Huang, R., Clarke, D. R., and Suo, Z., 2012, "Dielectric Elastomer Actuators Under Equal-Biaxial Forces, Uniaxial Forces, and Uniaxial Constraint of Stiff Fibers," *Soft Matter*, **8**(22), pp. 6167–6173.
- [23] Goulbourne, N., Mockensturm, E., and Frecker, M., 2005, "A Nonlinear Model for Dielectric Elastomer Membranes," *ASME J. Appl. Mech.*, **72**(6), pp. 899–906.
- [24] McMeeking, R. M., and Landis, C. M., 2005, "Electrostatic Forces and Stored Energy for Deformable Dielectric Materials," *ASME J. Appl. Mech.*, **72**(4), pp. 581–590.
- [25] Jhong, Y.-Y., Huang, C.-M., Hsieh, C.-C., and Fu, C.-C., 2007, "Improvement of Viscoelastic Effects of Dielectric Elastomer Actuator and Its Application for Valve Devices," *Proc. SPIE*, **6524**, p. 65241Y.
- [26] Palakodeti, R., and Kessler, M., 2006, "Influence of Frequency and Prestrain on the Mechanical Efficiency of Dielectric Electroactive Polymer Actuators," *Mater. Lett.*, **60**(29), pp. 3437–3440.
- [27] Keplinger, C., Kaltenbrunner, M., Arnold, N., and Bauer, S., 2008, "Capacitive Extensometry for Transient Strain Analysis of Dielectric Elastomer Actuators," *Appl. Phys. Lett.*, **92**(19), p. 192903.
- [28] Zhang, J., and Chen, H., 2014, "Electromechanical Performance of a Viscoelastic Dielectric Elastomer Balloon," *Int. J. Smart Nano Mater.*, **5**(2), pp. 76–85.
- [29] Zhao, X., Koh, S. J. A., and Suo, Z., 2011, "Nonequilibrium Thermodynamics of Dielectric Elastomers," *Int. J. Appl. Mech.*, **3**(02), pp. 203–217.
- [30] Park, H. S., and Nguyen, T. D., 2013, "Viscoelastic Effects on Electromechanical Instabilities in Dielectric Elastomers," *Soft Matter*, **9**(4), pp. 1031–1042.
- [31] Wang, J., Nguyen, T. D., and Park, H. S., 2014, "Electrostatically Driven Creep in Viscoelastic Dielectric Elastomers," *ASME J. Appl. Mech.*, **81**(5), p. 051006.
- [32] Lochmutter, P., Kovacs, G., and Wissler, M., 2007, "Characterization of Dielectric Elastomer Actuators Based on a Visco-Hyperelastic Film Model," *Smart Mater. Struct.*, **16**(2), pp. 477–486.
- [33] Yang, E., Frecker, M., and Mockensturm, E., 2005, "Viscoelastic Model of Dielectric Elastomer Membranes," *Proc. SPIE*, **5759**, pp. 82–93.
- [34] Wissler, M., and Mazza, E., 2007, "Mechanical Behavior of an Acrylic Elastomer Used in Dielectric Elastomer Actuators," *Sens. Actuators, A*, **134**(2), pp. 494–504.
- [35] Kollosche, M., Kofod, G., Suo, Z., and Zhu, J., 2015, "Temporal Evolution and Instability in a Viscoelastic Dielectric Elastomer," *J. Mech. Phys. Solids*, **76**, pp. 47–64.
- [36] Wissler, M., and Mazza, E., 2005, "Modeling and Simulation of Dielectric Elastomer Actuators," *Smart Mater. Struct.*, **14**(6), pp. 1396–1402.
- [37] Michel, S., Zhang, X. Q., Wissler, M., Löwe, C., and Kovacs, G., 2010, "A Comparison Between Silicone and Acrylic Elastomers as Dielectric Materials in Electroactive Polymer Actuators," *Polym. Int.*, **59**(3), pp. 391–399.
- [38] Suo, Z., 2010, "Theory of Dielectric Elastomers," *Acta Mech. Solida Sin.*, **23**(6), pp. 549–578.
- [39] He, T., Zhao, X., and Suo, Z., 2009, "Dielectric Elastomer Membranes Undergoing Inhomogeneous Deformation," *J. Appl. Phys.*, **106**(8), p. 083522.
- [40] Leng, J., Liu, L., Liu, Y., Yu, K., and Sun, S., 2009, "Electromechanical Stability of Dielectric Elastomer," *Appl. Phys. Lett.*, **94**(21), p. 211901.
- [41] Gent, A., 1996, "A New Constitutive Relation for Rubber," *Rubber Chem. Technol.*, **69**(1), pp. 59–61.
- [42] Reese, S., and Govindjee, S., 1998, "A Theory of Finite Viscoelasticity and Numerical Aspects," *Int. J. Solids Struct.*, **35**(26–27), pp. 3455–3482.
- [43] Schwarzl, F., and Staverman, A., 1953, "Higher Approximation Methods for the Relaxation Spectrum From Static and Dynamic Measurements of Viscoelastic Materials," *Appl. Sci. Res., Sect. A*, **4**(2), pp. 127–141.
- [44] Xiao, R., Guo, J., and Nguyen, T. D., 2015, "Modeling the Multiple Shape Memory Effect and Temperature Memory Effect in Amorphous Polymers," *RSC Adv.*, **5**(1), pp. 416–423.
- [45] Ferry, J. D., 1980, *Viscoelastic Properties of Polymers*, Wiley, New York.
- [46] Nguyen, T. D., Yakacki, C. M., Brahmabhatt, P. D., and Chambers, M. L., 2010, "Modeling the Relaxation Mechanisms of Amorphous Shape Memory Polymers," *Adv. Mater.*, **22**(31), pp. 3411–3423.
- [47] Haupt, P., Lion, A., and Backhaus, E., 2000, "On the Dynamic Behaviour of Polymers Under Finite Strains: Constitutive Modelling and Identification of Parameters," *Int. J. Solids Struct.*, **37**(26), pp. 3633–3646.
- [48] Foo, C. C., Cai, S., Koh, S. J. A., Bauer, S., and Suo, Z., 2012, "Model of Dissipative Dielectric Elastomers," *J. Appl. Phys.*, **111**(3), p. 034102.